Dual and Multi-Spectral Band SLS Infrared Camera Systems

Murzy Jhabvala[1,], Donald Jennings[1], Kyle Turck[2], Compton Tucker[1], Allen Lunsford[3], Christine Jhabvala[1], Analia Cillas[4], Joel Mccorkel[1], Jason Hair[1], Doug Morton[1], Dong Wu[1], Markus Loos[5], Fred Wang[1], Tilak Hewagama[1], Sachidananda Babu[1], Mani Sundaram[6], Jason Bundas[6], K.K. Choi[7], Corey Tucker[7]*

[1]NASA Goddard Space Flight Center, Greenbelt, Maryland USA
[2] Global Science and Technology Greenbelt, Maryland USA
[3]American University, Washington, D.C. USA
[4] Univ. of Maryland, Baltimore County, Maryland, USA
[5]Markury Scientific, Inc., Thousand Oaks, California USA
[6]QmagiQ, LLC, Nashua, New Hampshire, USA
[7]SSAI, Greenbelt, Maryland, USA

** Corresponding author: murzy.d.jhabvala@nasa.gov*

ABSTRACT

Based on the recent success of our strained-layer superlattice (SLS)-based infrared (IR) camera that performed Earth imaging from the International Space Station (ISS) in 2019 we have built, what we consider, to be the next generation multi-band SLS imaging system. The Compact Thermal Imager (CTI) was installed on the Robotic Refueling Mission 3 (RRM3) and attached to the exterior of the ISS. From this location we were able to capture 15 million images of a multitude of fires around the globe in 2019. This unexpected trove of data initiated quite a bit of scientific interest to further utilize this imaging capability but would include features to more precisely monitor terrestrial fires and other surface phenomena. To this end, we developed a technique to install specific bandpass filters directly onto the SLS detector hybrid assembly. Utilizing this technique we have built a CTI-2 camera system with two filters, 4 and 11µm, and have made a second detector assembly with six filter bands from 4-12µm. This second system will also be used to supplement Landsat remote imaging monitoring approximate land surface temperatures, monitor evapotranspiration, sea ice and glacier dynamics. The CTI-2 camera is based on a 1,024x1,024 (1kx1k) format SLS detector hybridized to a FLIR ISC0404 readout integrated circuit (ROIC). The six band SLS focal plane array is based on the 640x512 FLIR ISC 9803 ROIC. This camera system is based on the Landsat 8 and 9 Thermal IR Sensors (TIRS) instrument and one of its purposes is to perform ground truthing for the Landsat 8/9 data at higher spectral resolution. Both Landsat TIRS instruments are dual band thermal IR sensors centered on 11 and 12µm (each with about a 1µm bandpass). Both of our SLS systems utilize a Ricor K548 cryocooler. To streamline costs and development time we used commercial optics and both commercial and custom NASA electronic components. A primary feature of these camera systems is the incorporation of specific filters to collect fire data at ~3.9µm and thermal data at ~11µm. The CTI-2 instrument is designed for 37 m /pixel spatial resolution from 410km orbit (ISS orbit). In this paper, we will present the design and performance of the focal plane, optics, electronics and mechanical structure of the dual-band CTI-2 and the focal plane performance of the six-band focal plane.

Keywords: IR detectors, SLS detectors, bandpass filters

1. INTRODUCTION

The Compact Thermal Imager (CTI) was successfully launched on December 5, 2018 [1] on the SpaceX 16th Commercial Resupply Services (CRS-16) mission on board the NASA Robotic Refueling payload. Rendezvous with the International Space Station (ISS) occurred on December 8th, 2018. The primary goal was a space-based demonstration of the SLS detector technology which would then qualify this emerging detector family for future NASA space-flight missions. There were a number of other novel features we also wanted to space qualify, or in NASA terms, raise the technology readiness level (TRL) above TRL-6. A successful space-borne mission generally qualifies the instrument to TRL-9 (our goal). This goal was met for this instrument but beyond the technology qualification the CTI was an operational dual-band IR imager on the ISS capturing over 15 million images during 2019[2]. This was an entirely unexpected and surprising outcome that yielded an enormous amount of earth imagery and specifically images of wildfires across the globe in two electrically selectable IR bands: 3.3–5.4µm and 7.8-10.2µm [3,4]. The SLS detector in the CTI was a 320x256 format array with 30µm pixels hybridized to a FLIR ISC0903 ROIC [5]. The spatial resolution was 80m/pixel from the ISS. This data has and continues to be analyzed by a team of NASA scientists and engineers ever since the first images were returned more than 3 years ago. A photograph of the CTI instrument is shown in Figure 1 and an image of a region of the Amazon where there were many fires overlayed on a Google Earth image.

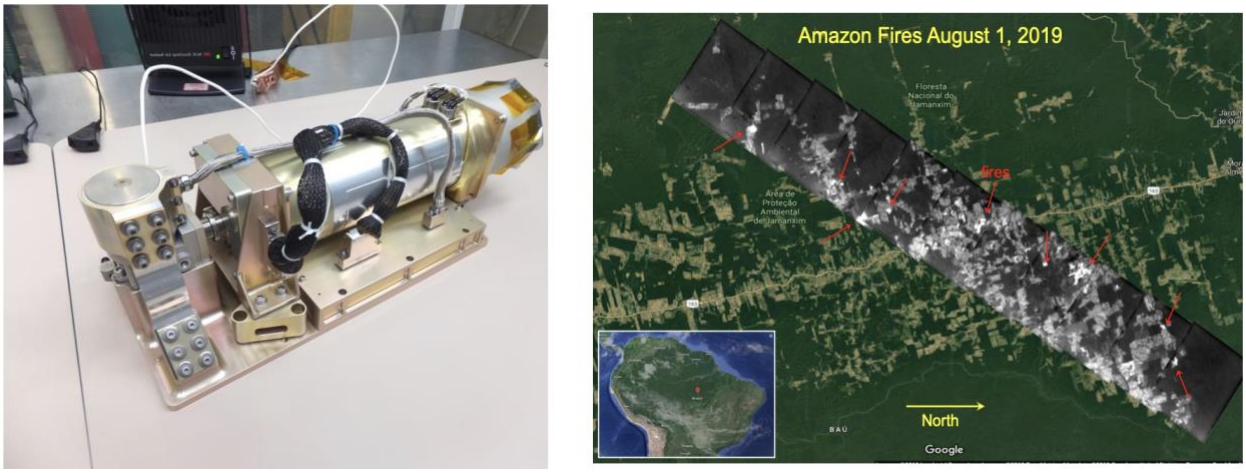

Figure 1. Left; The Compact Thermal Imager instrument which was installed on the NASA Robotic Refueling payload aboard the International Space Station in 2019. Right; One of over 15 million images collected by CTI. During late Summer 2019 a large number of fires were started in the Amazon rainforest. On August 1, 2019, CTI flew over Novo Progresso in the state of Pará in northern Brazil where fires have been particularly common. Novo Progresso is located along north-south route BR-163, where much deforestation has taken place in recent years. CTI identifies fires by their excessive brightness in infrared images. In the picture, infrared imagery appears gray and fires are indicated with red arrows. Several of the burning areas are quite large, approaching 1 kilometer across. The smallest fires appear in single 80-meter pixels. The locale where these fires were found shows evidence of extensive clearing of vegetation.

Concurrent with this analysis new instrument concepts have been formulated to further improve on the science return pertaining to wildfires, biomass burning, emitted aerosols, measurements of ice sheet, glacier and snow temperatures, plus measurement of plant and soil surface temperatures from evapotranspiration and cloud parameters. The next generation CTI-2 instrument will have a spatial

resolution of 35m/pixel from the ISS, utilize a 1kx1k format SLS array and contain two optically filtered bands, each band covering ½ of the array. Instead of the K508 Ricor cooler [6], CTI-2 uses the slightly more powerful K548 Ricor cooler. Direct attachment of the filter to the detector hybrid is a new innovation recently implemented by the Goddard detector development group in Greenbelt, Maryland. This filter attachment method was also used to build a 640x512 SLS focal plane that contains a 6-band butcher block filter, also directly mounted to the detector hybrid. This 6-band focal plane array will be installed into a portable, ground-based/airborne imaging system. As a result of successful SLS-based instruments numerous opportunities have emerged. The advantages of SLS have broad appeal. The relative ease and consistency of fabrication; broad spectral response; warmer operating temperature compared to the precursor quantum well photodetectors; higher quantum efficiency all contribute to its versatility and relative affordability particularly for high background applications such as earth, lunar, planetary, asteroid/comet imaging science missions. We continue to innovate with this technology to meet both NASA and commercial applications, particularly in the area of fire science. In this paper we describe the development and performance of the CTI-2 instrument and the 6-band focal plane array.

I. The Dual-band CTI-2 SLS Focal Plane Array

Prior to installing the dual-band filters onto the 1kx1k detector hybrid we performed a full characterization of both the detector and of the filter assemblies. The detector tests included: dark current vs temperature, noise performance, relative spectral response and absolute quantum efficiency, full well, power dissipation, noise equivalent temperature difference and a variety of external imaging experiments. Prior to installing the dual-band filter on the detector we measured the filter spectral transmittance. The filter measurements, covering from 2.0–13µm, were performed with a Fourier transform spectrometer. Shown below in Figure 2 is a photograph of the filter installed on the detector hybrid (after the detector was characterized) and the filter transmission for each band.

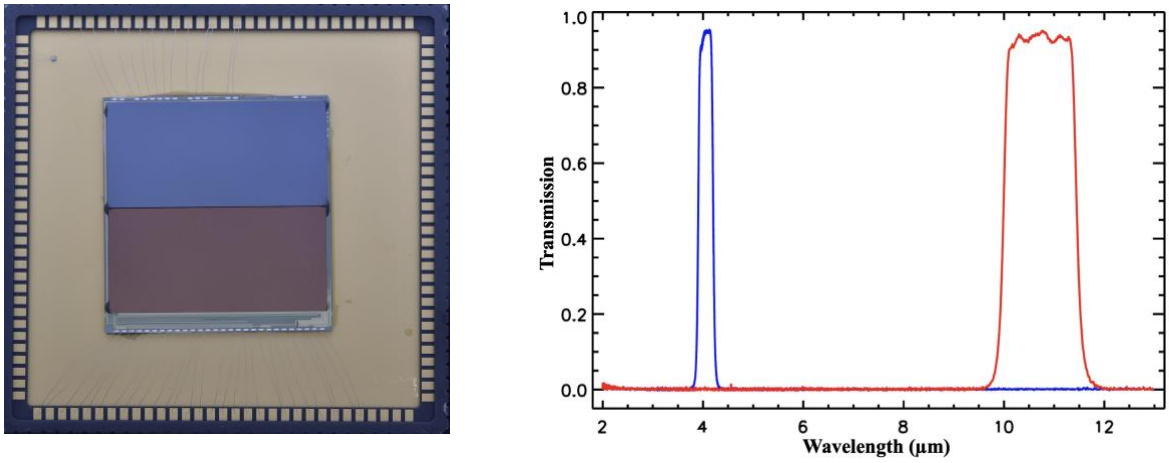

Figure 2. Left; photograph of the 1kx1k detector hybrid with the two filers attached. Right; measured transmission of each filter prior to attaching to the detector hybrid. The center wavelengths are 3.975µm with a bandwidth of 0.3µm and 10.75µm with a bandwidth of 1.5µm.

The array was tested by taking a focused image of a soldering iron as seen in Figure 3. The detector is first thoroughly characterized before committing to the filter attachment. Custom filter assemblies can be quite expensive with limited commercial availability. The background-subtracted soldering iron image confirmed the adequacy of the array and suitability for further comprehensive performance testing and subsequent filter installation. Tests performed on the detector include: dark current versus temperature and detector bias; relative spectral response and absolute quantum efficiency; full well capacity; noise performance; noise equivalent temperature difference power dissipation and some array pixel statistics.

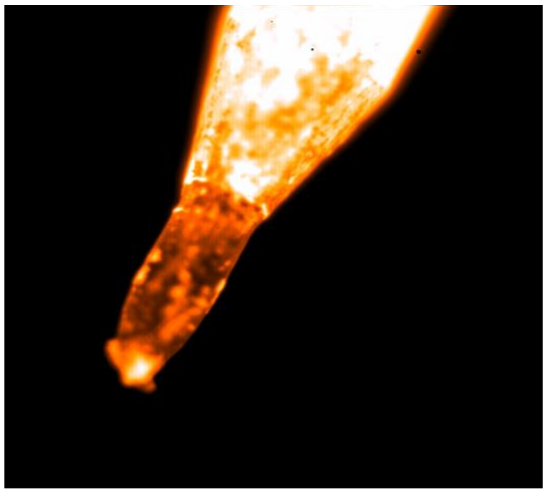

Figure 3. Broadband infrared image of a soldering iron at T=80K. This image was taken during the initial test of the detector array prior to installing the filter.

A. Dark Current

Dark current images were collected with detector bias voltage of 0.2V at each of the following temperatures: 70K, 80K, and 85K. The dark current is measured by taking several dark exposures at different exposure times and plotting the dark signal versus the exposure time for each pixel. Assuming a gain of 258.5 electrons per A/D unit (ADU) based on the node capacitance of the ISC0404 input amplifier the signal is converted into electrons (e-). Figure 4 shows a plot of signal vs integration time at a bias voltage of 0.2V and detector temperature of 70K and the entire 1 megapixel dark current image map. Figure 5 and Table 1 show the median dark current at all four temperatures.

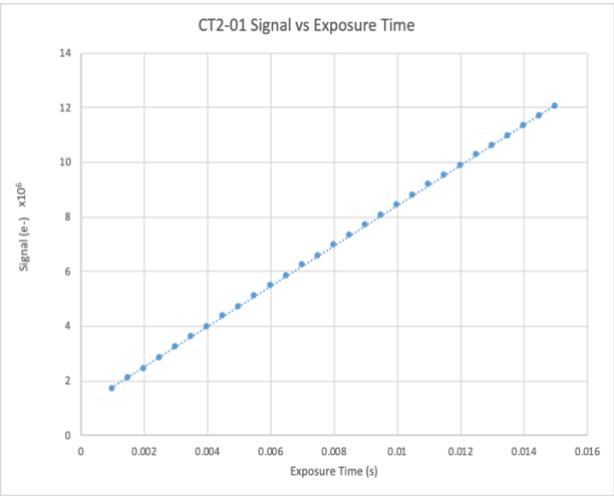

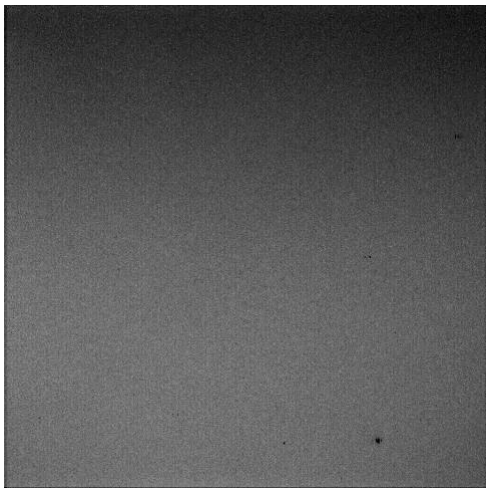

Figure 4. Left: Dark current calculation at 0.2V bias and a temperature of 70K using linear regression of signal accumulation vs exposure time. Right: Dark image calculated from a linear regression of dark exposures at 0.2V bias and a temperature of 70K. Darker areas in the image indicate lower dark current.

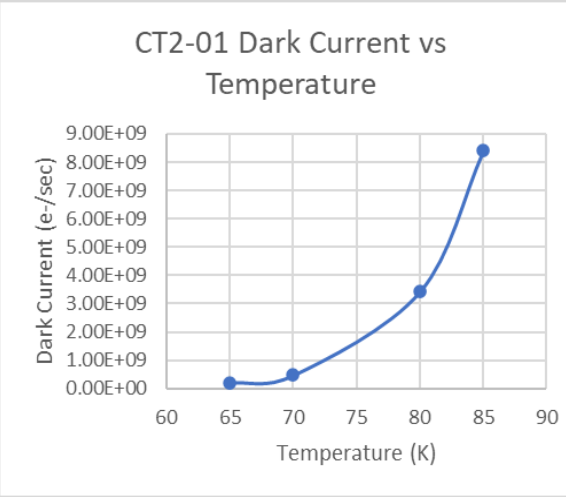

Figure 5. Median dark current vs. temperature for the entire array.

Table 1
Median I_D vs. T for the entire array

Detector Temperature (K)	Dark Current (e-/s)
65	2.00E+08
70	4.69E+08
80	3.43E+09
85	8.41E+09

B. Quantum Efficiency

Both the relative response and absolute quantum efficiency (QE) were measured by exposing the SLS array to flat field illumination from a blackbody radiation source. The absolute QE data was collected using a blackbody radiation source operating at 800°C with an emissivity of better than 0.97, and a dewar window transmittance of 0.93.

Relative response measurements were first made using a SpectraPro 300i monochromator with a 1000ºC blackbody source. Measurements were taken with 50 nm resolution over the wavelength range from 1-15 µm with Gen 3 Leach electronics. Spectral power distribution at the monochromator output was measured with a calibrated model FTIR16-2 HgCdTe detector whose absolute accuracy is ~5%. At each wavelength, the output of the monochromator was measured with the calibrated detector and then with the SLS detector array. The detector output signal was divided by the transmittance of the dewar window and compared to the calibrated detector measurement to provide a calibrated relative response at each wavelength. The effect of atmospheric transmittance was considered negligible over the short path lengths used in the measurements. The broadband absolute spectral response measured prior to installing the two bandpass filters. After all the tests were completed and the detector assembly removed from the dewar the custom dual-band filter was attached and the detector was again characterized primarily focusing on the filtered spectral response. The absolute spectral response was again measured and the other characteristics spot checked to ensure pre-filter attachment performance was the same. Shown below in Figure 6 are the QE before and after installation of the dual-band filter.

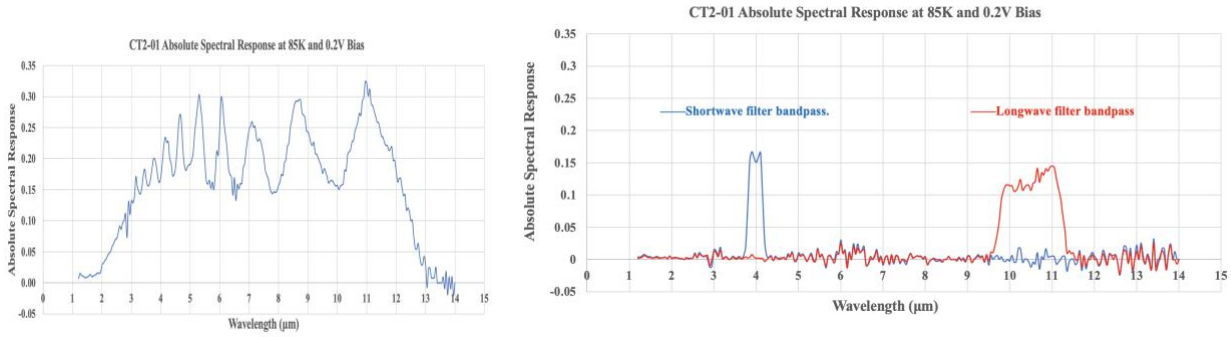

Figure 6. Left; the absolute spectral response of the detector prior to the filter installation. Right; the filtered detector absolute spectral response. Both measurements were taken at T=85K and 0.2V detector bias.

C. Noise Performance

To calculate the noise per pixel, a short dark exposure of 100 µs integration time containing 100 frames was collected. The difference between consecutive frames were subtracted. The standard deviation of those differences was calculated per pixel, and the conversion gain of 258.5 electrons per ADU was applied. As seen in Figure 7 and the accompanying table, the noise for the array increases with an increase in temperature. This increase in noise is expected because the dark current signal, and therefore the dark shot noise, increases with temperature. The numbers below have not been corrected for the dark shot noise and should therefore be viewed as an upper limit of the read noise. The read noise for the ISC 0404 ROIC is specified as -85 db of the full well signal of ~13 million electrons (see next section). This corresponds to 731electrons. The corresponding dark current shot noise at 80K for a 1ms integration interval is 583 electrons so the system noise of 1277 electrons is somewhat higher than the expected 935 electrons, due to the excess noise contributed by the cryogenic test system. The median noise versus temperature is listed in Table 2.

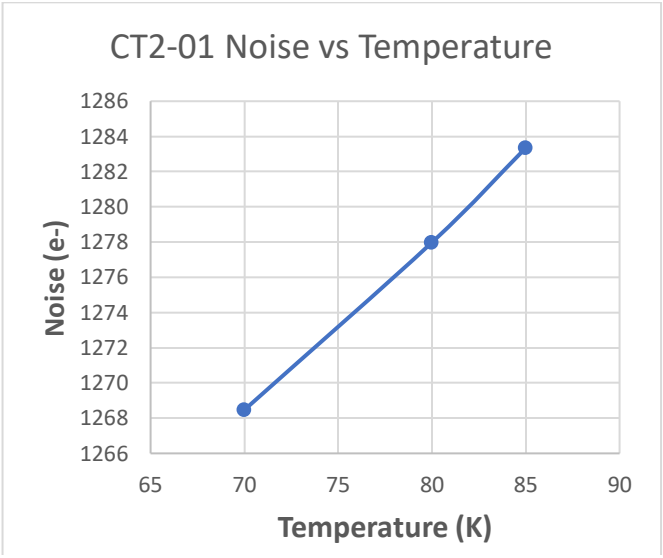

Figure 7. Median noise vs. temperature for the entire array.

Table 2
Median Noise vs. T for the entire array

Detector Temperature (K)	Noise (e-)
70	1268.47
80	1277.98
85	1283.35

D. Full Well

The full well for this hybrid was calculated by taking dark images at increasing exposure times until saturation was reach at ~13E6 electrons. Figure 8 shows this dark current data up to that saturation level.

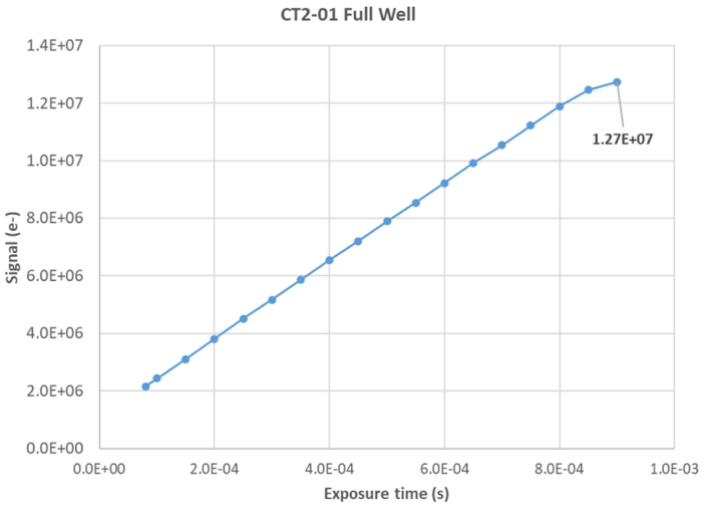

Figure 8. Dark signal vs exposure time. Saturation occurs at around 0.85 ms corresponding to ~13 million electrons.

E. Non-Functioning Pixels

The non-functional pixels were determined with a similar method to the one used in the dark current test except the detector was exposed to a constant 800°C blackbody source rather than a cold shutter. The pixel responses to the blackbody were then recorded at increasing exposure times. The slope of the pixel response (e-) vs the exposure time (s) would then be the response rate (e-/s) and was calculated using a linear regression. The pixels with response rates of zero e/s or less are considered to be "dead" nonfunctional pixels and the pixels with response rates greater than 5E10(e-/s) are considered to be "hot" nonfunctional pixels. There are 1363 pixels that are nonfunctional corresponding to a "good" pixel yield of 99.87%. In many scientific instruments the range of "acceptable pixels would likely have more stringent requirements even though they are functioning. In past instruments acceptable pixels had to have a dark current and noise less than a prescribed value, a QE greater than a certain value and fall with a narrow range of spectral response uniformity. The 99.87% yield here is the "best case". Depending on the science requirements some of the good pixels may excluded from the data analysis.

F. Power Dissipation

The detector voltages were measured for a number of bias voltages with GEN3 electronics operating in 8-channel mode. Voltages were taken at each bias voltage in the dark configuration. The results are shown in the adjacent Table 3.

Table 3
Detector/ ROIC Power Dissipation at T=85K and Detector Bias of 0.2 volts

Bias Line	Voltage (V)	Power (mW)
Vdet_adj	2.32	0
Voutref	1.02	0
Vpos	3.58	41.2
Vposout	3.58	25.9
Vpd	3.58	1.04
TOTAL		68.0

II. The Multi-Band SLS Focal Plane Array

We followed the same procedure in the 6-band detector hybrid as in the dual-band hybrid described in the previous sections. However, this detector was a 640x512 format array with 25µm^2 pixels. The array is hybridized to a FLIR ISC9803 ROIC. The first test is to make sure the detector is functioning adequately before committing to the filter attachment. To convince ourselves that the detector was suitable we only performed a quick imaging test in our rapid turn-around cryogenic test chamber. No detailed testing was performed at this time. Shown in Figure 9 is a photograph of the detector hybrid

with the 6-band filter attached in the test system and two IR images of a soldering iron, unpowered and then powered.

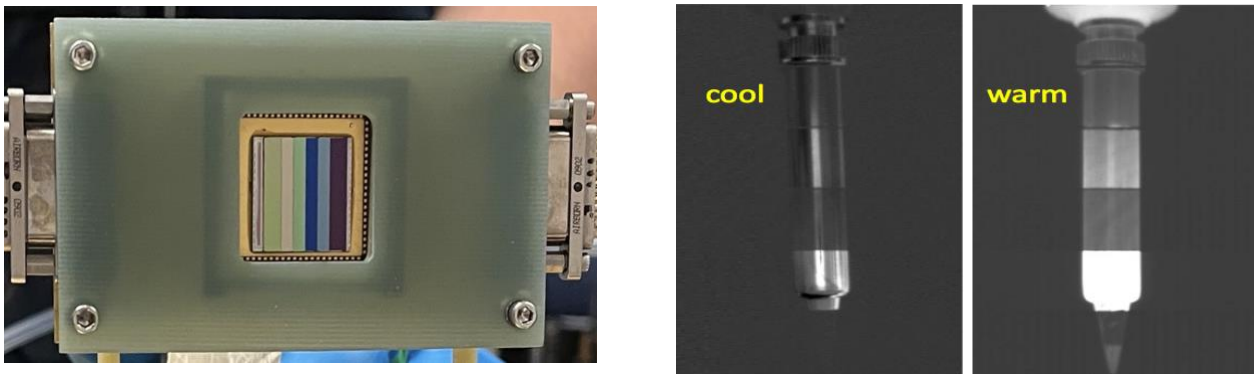

Figure 9. Left: Image of the detector with attached filter ready to be tested. Right: Two six band IR images of a soldering iron. The heated tip of the soldering iron is visible in the bottom 4µm band one whereas it is not at all visible in the unpowered or cool soldering iron image.

As before, tests performed on this detector include: dark current versus temperature and detector bias; relative spectral response and absolute quantum efficiency; full well capacity; noise performance; noise equivalent temperature difference power dissipation and some array pixel statistics. The test procedures were, for the most part, identical to those described in the previous sections starting with dark current. Prior to installing the butcher block filter onto the detector hybrid we again performed transmission measurements of each band. The Goddard test results corresponded precisely with the results reported by the filter vendor. The measurements performed at Goddard are shown in Figure 10.

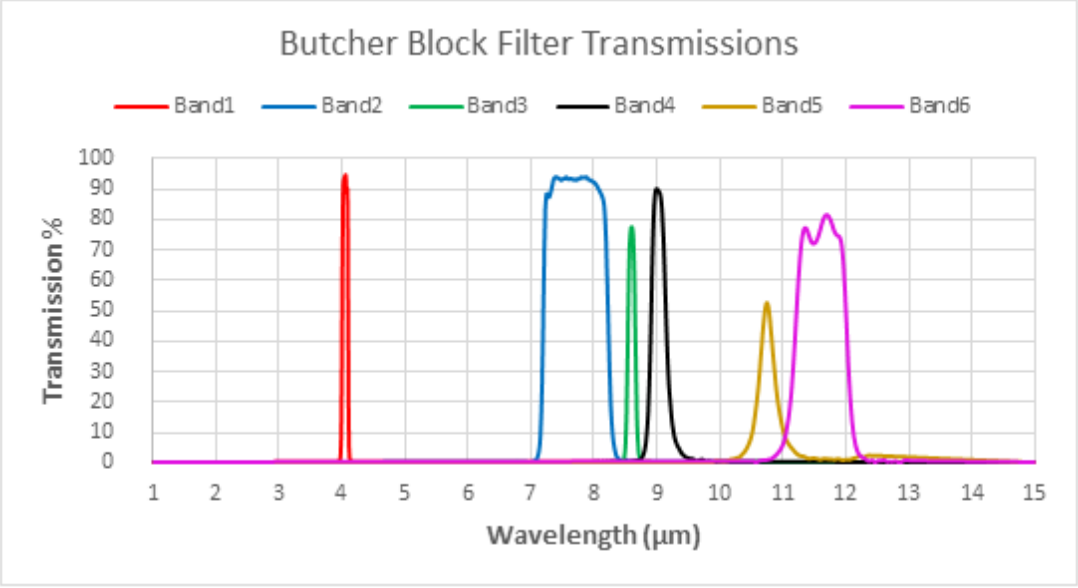

Figure 10. Measured 6-band filter transmission prior to installation on the detector.

A. Dark Current

Dark images were collected with a detector bias voltage of 0.2V and a detector temperature of 70K. Dark images of several different integration times were used to measure the signal vs. the exposure time for the SLS array. Figure 11 shows a dark current difference-image between exposures of 3 and 2 ms. The dark current is again measured by plotting the dark signal versus the exposure time as shown in Figure 12. Analysis reveals two separate regions where the dark increases linearly with exposure time. We attribute this to a change in gain with signal that occurs in the ROIC where the integrating capacitor changes by a factor of 4. Avoiding the transition region, we fit two lines, one at high signals assuming a gain of 151 electrons/ADU based on the node capacitance of the input amplifier and one at low signals assuming a gain of 40.5 electrons/ADU. These separate measurements yield the same dark current to within about 5%. Figure 13 shows the median dark current for each filter band. Analysis reveals two separate regions where the dark increases linearly with exposure time. We attribute this to a change in gain with signal that occurs in the ROIC where the integrating capacitor changes by a factor of 4. Avoiding the transition region, we fit two lines, one at high signals assuming a gain of 151 electrons/ADU based on the node capacitance of the input amplifier and one at low signals assuming a gain of 40.5 electrons/ADU. These separate measurements yield the same dark current to within about 5%.

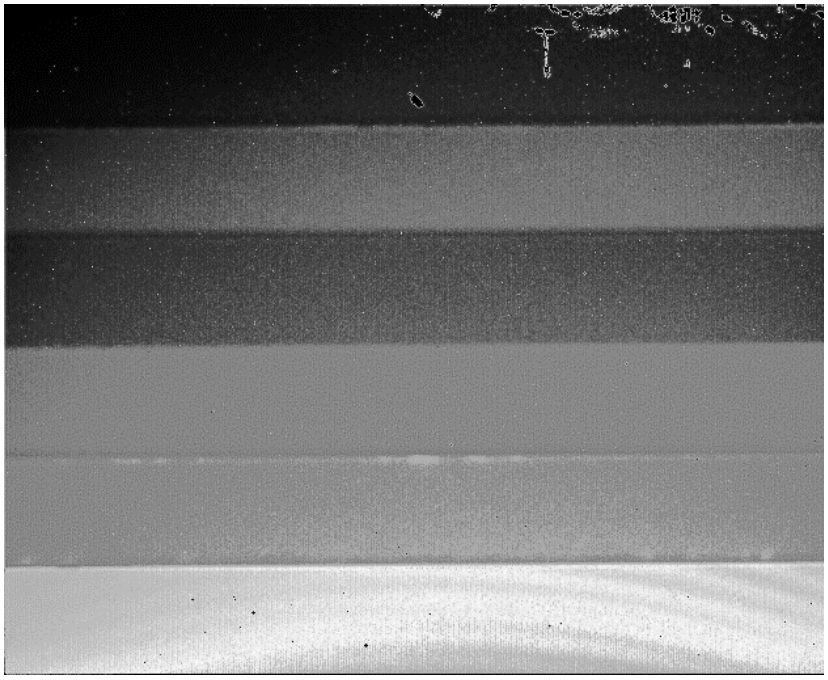

Figure 11. Dark image resulting from the difference of 3ms and 2ms dark exposures. Darker areas in the image indicate lower dark current.

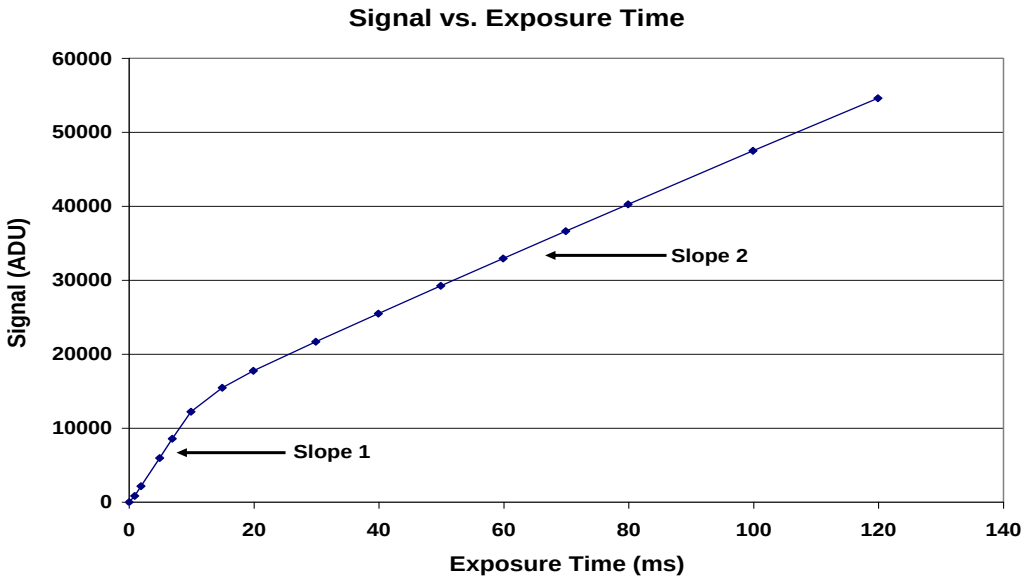

Figure 12. Dark signal versus the exposure time, Two regions are identified with different slopes for this particular ROIC.

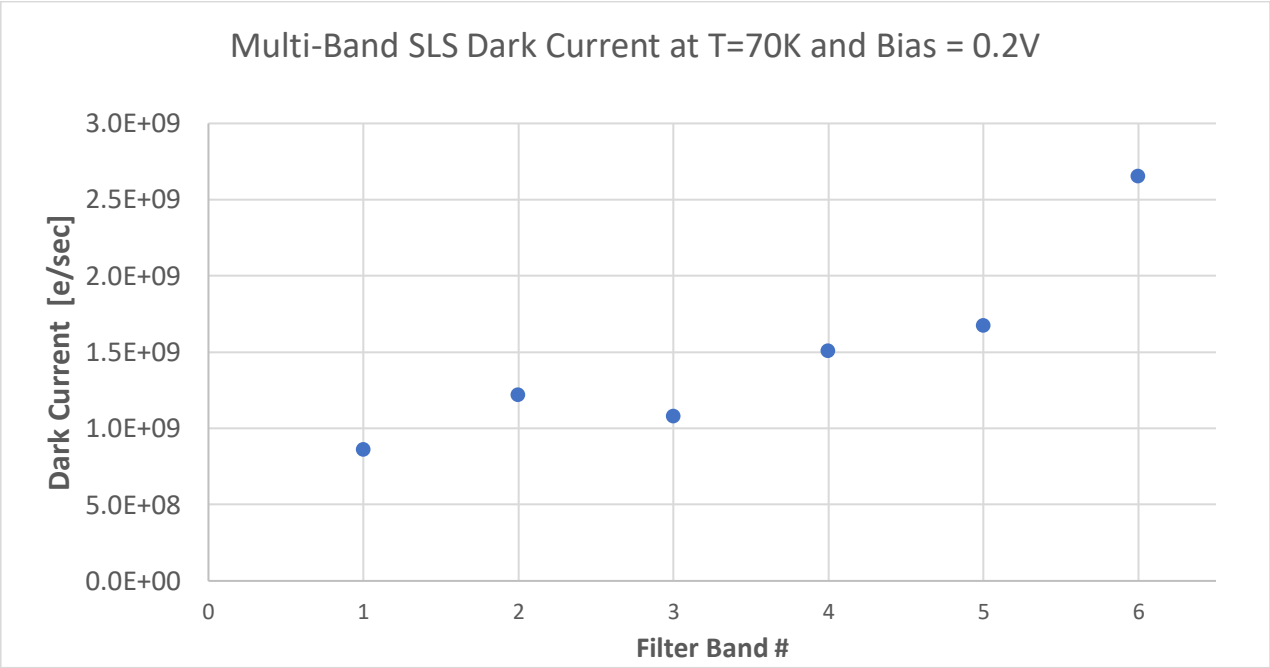

Figure 13. Median dark current for each filter band—refer to Figure 10.

A. Relative Response and Absolute Spectral Quantum Efficiency

Both the relative response and absolute quantum efficiency (QE) were again measured by exposing the SLS array to flat field illumination from a blackbody radiation source after the filter was attached. The absolute QE data was collected using a blackbody radiation source at 1053°C. The spectral quantum efficiency of each filter segment is shown below in Figure 14.

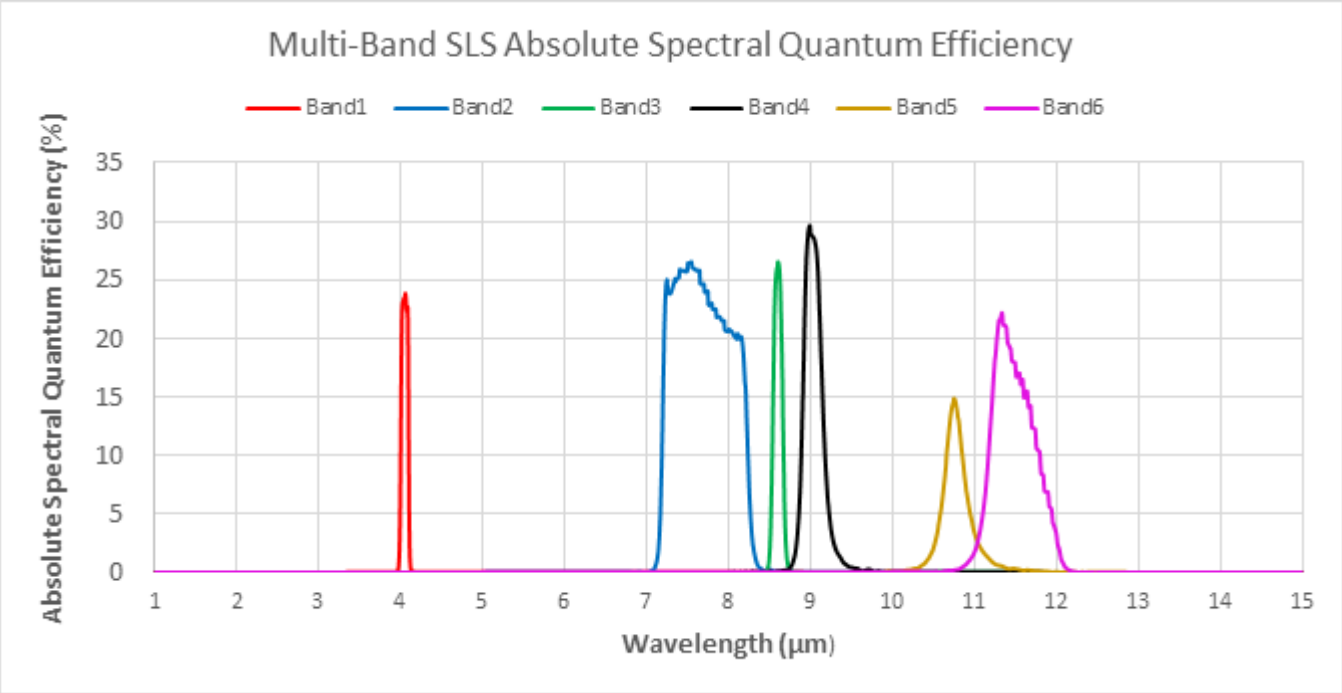

Figure 14. Spectral quantum efficiency of the six filter bands at a temperature of 75K and bias of 0.2V.

B. Noise Performance

As before, to calculate the noise per pixel, a short dark exposure of 100 µs containing 100 frames was collected. The standard deviation per pixel over the 100 frames is multiplied by a conversion gain of 40.5 electrons per ADU. The results for all bands are displayed in Figures 15 and 16. The read noise for the ISC 9803 ROIC is specified as 550 electrons. The corresponding dark current shot noise at 70K for a 1ms integration interval is, on average, electrons so the system noise of 1225 electrons similar to the previous noise measurement and indicative of the system noise that is in excess to the detector hybrid expected noise.

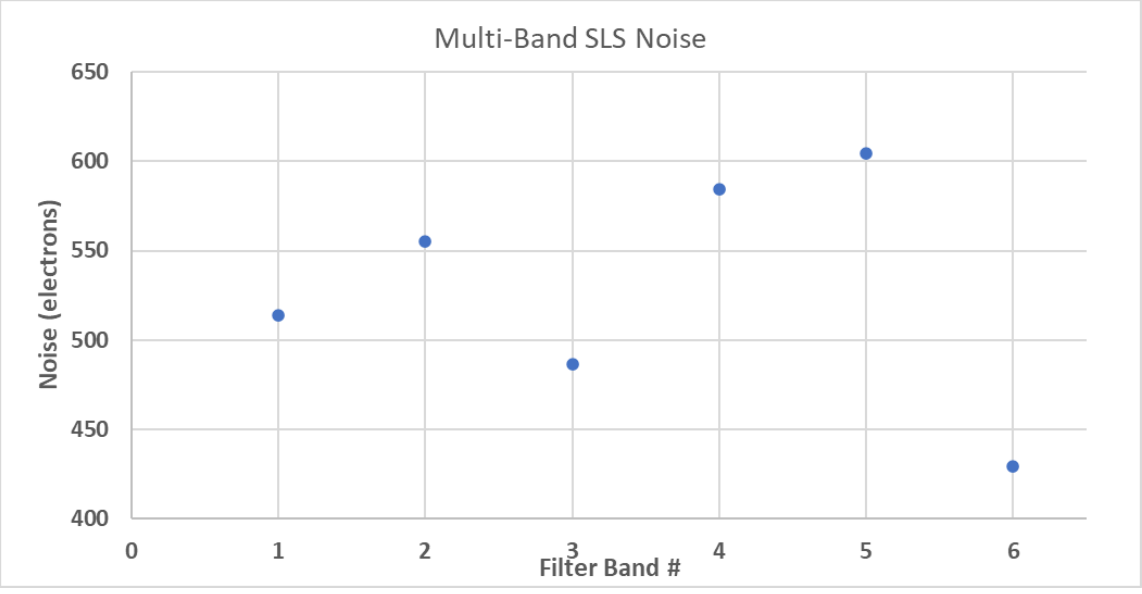

Figure 15. Median noise per pixel of short exposure time for each filter band at a temperature of 70K and bias of 0.2V.

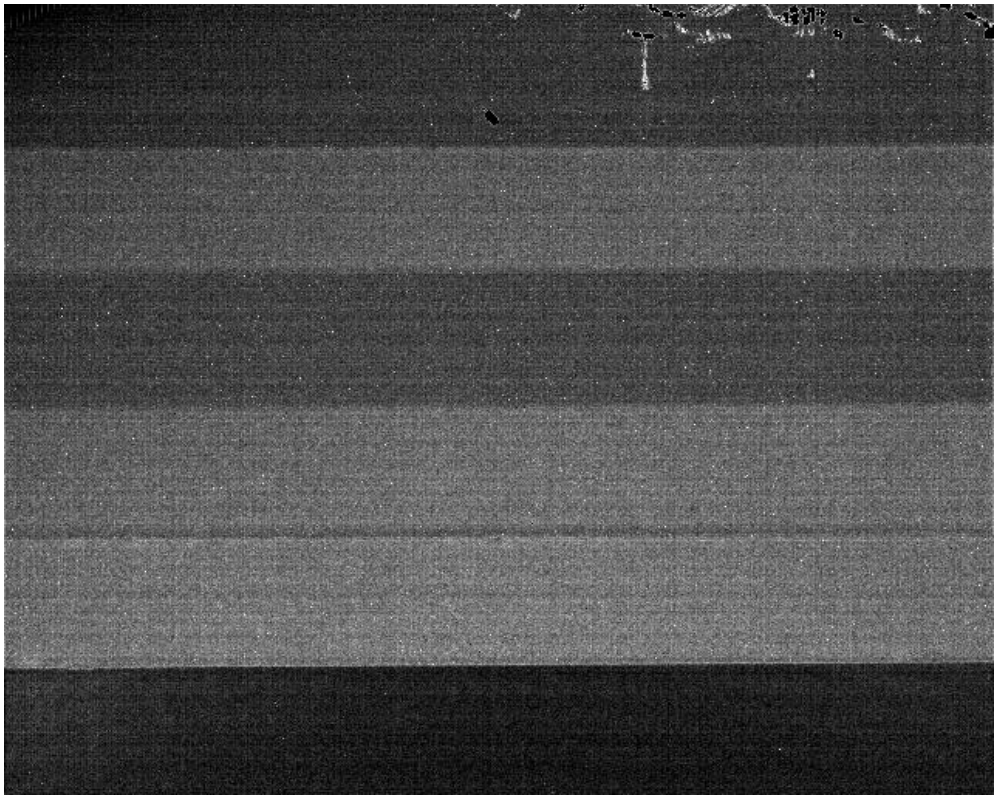

Figure 16. Noise per pixel in electrons (the lighter pixels have a higher noise value).

D. Power Dissipation

The detector voltages were measured together with the bias voltages with GEN3 Leach electronics operating in 4-channel mode while illuminated with the 300K background. The power dissipation through the Vdetcom bias increases by ~8mW compared to the dissipation when the background is shuttered. The power dissipation for the bias lines of the ISC9803 ROIC is shown in the adjoining table.

Power dissipation
Bias Voltage 0.2V while illuminated

Bias Line	Voltage (V)	Power (mW)
Vdetcom	5.960	8.844
Vref	1.627	0.000
Vpd	5.597	5.587
Vpos	5.604	62.586
Vposout	5.604	71.162
TOTAL		148.18

III. Second Generation Compact Thermal Imager (CTI-2)

Building on the success of CTI, we constructed a camera using the 1kx1k SLS array integrated with the dual-band filter described in Section I. The goal of this second-generation thermal camera, CTI-2, was to significantly improve imaging and spectral performance from orbit. The main science-driven objectives were: 1) to achieve a ground resolution of 40 m or better from the ISS orbit of 410 km and 2) provide a fire detection band at the 4 μm wavelength and a thermal band near 10 μm. The band at 4 μm coincides with an atmospheric spectral window that is short of the emission wavelengths of typical 300K

surface temperatures and is therefore especially sensitive to the high temperatures of fires. The 10 μm band is near the peak of the 300 K Planck emission and thus provides sensitive thermal imaging of typical ground scenes. Our aim was to build an instrument that met these objectives and to demonstrate its performance in the laboratory, in the field, and from airborne and flight platforms. The configuration of CTI-2 is shown in Figures 17 and 18. A summary of the CTI-2 system is presented as a block diagram in Figure 21. An overall schematic of the system is shown in Figure 19. By taking advantage of the larger number of pixels, smaller pixel size and a longer focal length telescope, CTI-2 delivers a pixel resolution more than a factor of two better than that of CTI and covers a ground swath 46% wider. In CTI-2, a 200 mm focal length, f/2 telescope is coupled to the Integrated Dewar Cooler Assembly (IDCA). The telescope, supplied by Stingray Optics, LLC., is a 100 mm aperture diameter catadioptric device chromatically corrected over the 3-12 mm wavelength range. The telescope was subsequently modified for use in space. The IDCA, assembled by American Infrared Solutions (AIRS), includes a Ricor 548 mechanical cooler with a dewar vacuum housing in which the detector/filter assembly is mounted. Infrared light from the telescope enters the dewar through a ZnSe window. Commanding the detector ROIC and reading out data are performed with a SIDECAR ASIC (Systems Image, Digitizing, Enhancing, Controlling, And Retrieving Application-Specific Integrated Circuit), manufactured by Teledyne Technologies, Inc. Control of the SIDECAR is provided through a MACIE interface board (Markury ASIC Control and Interface Electronics) manufactured by Markury Scientific, Inc.

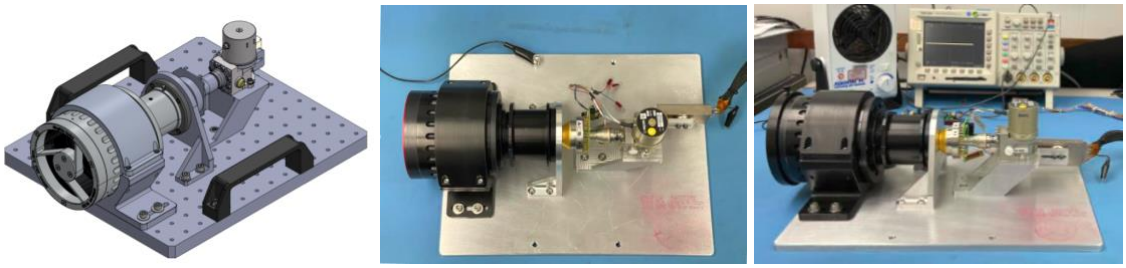

Figure 17. Views of the CTI-2 conFigured for laboratory and field use. Top: Mechanical drawing of assembly. Middle and lower: Views of assembly from above and side. The IDCA assembly, consisting of the dewar, cryocooler and SIDECAR ASIC [7] are on the right. The dewar housing with the detector and filters is in the middle and the telescope is on the left (black housing). Optical ray traces are super-imposed.

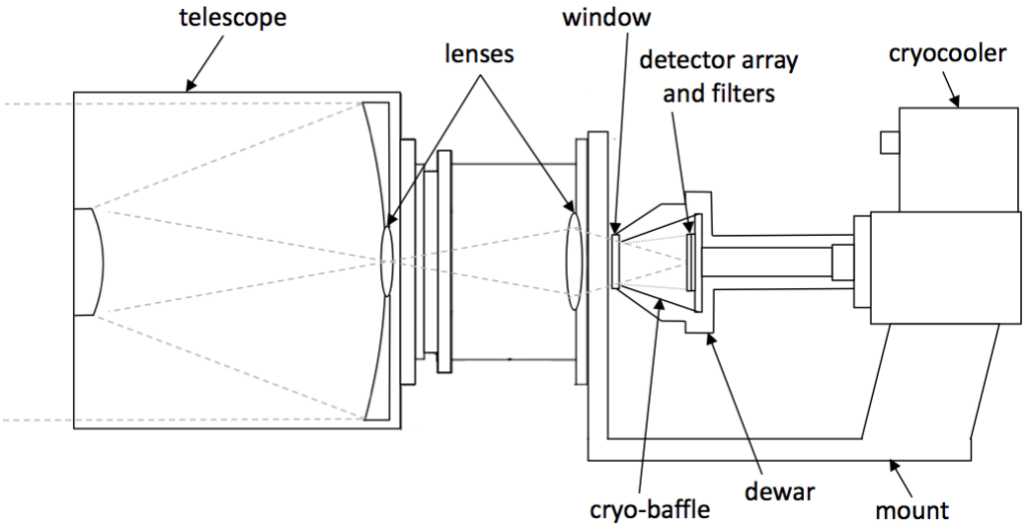

Figure 18. Conceptual schematic of optical-mechanical design of CTI-2. The telescope (including catadioptric lenses) is coupled to the IDCA (cryocooler/dewar/focal plane assembly) with an interface mount.

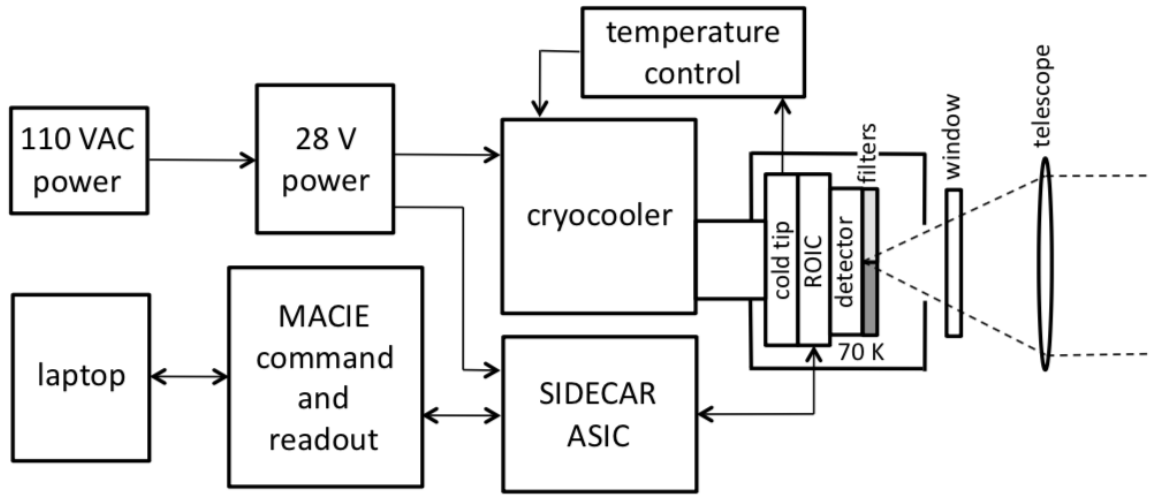

Figure 19. Schematic of CTI-2 configured for and laboratory and field work.

The instrument parameters listed in Table 4 meet the science objectives. The spectral transmission of the two filter segments were measured both at room temperature and at cryogenic temperature, as described in Section l. A small blue shift of the filter wavelengths was introduced by cooling. The bandpasses listed in Table 4 are for the focal plane operating temperature. These operating parameters depend somewhat on the type of observation to be made. Digital files uploaded to SIDECAR establish the operating mode of the detector hybrid. An orbital altitude of 410 km was chosen as a benchmark for comparison with CTI on ISS. This sets the ground resolution; a pixel resolution of 37 m per pixel from 410 km altitude would correspond to 63 m from 700 km altitude. Swath width, frame time, data rate and NEDT also depend on altitude (NEDT depends on pixel dwell time). Some parameters, integration time in particular, are independent of the altitude or range. Integration time is chosen based on the dark current, so that signal-plus-dark current fills the ROIC charge wells without saturation. Cold spectral filters increase integration time by reducing the background flux. Other operating modes, such as the single-row readout are discussed below.

CTI-2 was assembled in stages. As described above, the detector hybrid was first characterized as a bare unit, without filters, in a laboratory test dewar. The dual-bandpass filter was then attached to the detector. This combined focal plane unit was then re-measured for overall quantum efficiency, (spectral response). Following laboratory characterization, the focal plane was provided to AIRS for assembly of the IDCA. The focal plane unit – detector, ROIC and filter – was mounted on the cold-tip inside the dewar housing of the cryocooler. The IDCA provided a connector for coupling the focal plane to the SIDECAR, which was in turn interfaced to the MACIE board. A laptop computer provided command and data readout capability through the MACIE. A separate power supply provided 28 volts to the SIDECAR and cryocooler. A mount assembly was constructed to rigidly hold the telescope at the focal distance from the detector array. Coarse adjustments of the focus could be made with bolts in slotted holes and fine adjustments with shims.

CTI-2 was calibrated in the laboratory using the same techniques as were used for CTI, described by Jennings et al. (2021). To adjust the focus an image of a pinhole was projected onto the focal plane by a reverse telescope. The reverse telescope was set to simulate a source at infinity, so that the nominal focus of CTI-2 was for long distant viewing. We found a 0.36 mm shift in optimum focus between the two

filter segments. The shift was found to be due to a difference in indices of refraction between the 4 μm sapphire filter and the 10.5 μm germanium filter.

Instrument response was calibrated by viewing a warm blackbody panel set at temperatures from room temperature, nominally 22 C, to 60 C. In the 10.5 μm band with an integration time of 0.5 msec we measured a baseline response of 19,400 analog-to-digital (A/D) counts at 22 C and a change of 145 counts per one degree C increase in blackbody temperature. In the 4 μm band with a 2.5 msec integration time we measured a response of 1850 A/D counts at 60 C and a change of 60 A/D counts per degree C increase.

Table 4. CTI-2 Instrument Parameters

SLS array format	1024x1024 pixels	Telescope[1] focal length	200 mm
Pixel size	18 μm	Telescope lens diameter	100 mm
Dark current	$1x10^9$ e^-/sec	Telescope temperature	20 C
Read noise	1270 e^-	Pixel IFOV	18.6 arcsec
ROIC well capacity	$1.3x10^7$ e^-	Pixel A Omega	$6.4x10^{-7}$ cm^2str
Bias	0.2 V	Array FOV	5.28 x 5.28 deg^2
Detector temperature	73 K	Band FOVs	5.28 x 2.64 deg^2
Band 1 coverage	3.78-4.15 μm	Altitude	410 km
Band 2 coverage	9.73-11.28 μm	Pixel ground IFOV	37 m
Band 1 integration time	2.5 msec	Band ground FOV	38x19 km^2
Band 2 integration time	0.5 msec	Cryocooler	Ricor K548
Frame time on orbit	2 seconds	Cryocooler Power (@28 V)	12 W
Data rate	8.4 Mbits/sec	ASIC	SIDECAR
Band 1 NEDT	<1 K @500 K	Electronics Interface	MACIE
Band 2 NEDT	<0.2 K @296 K	Mass	8 kg

\

IV. Examples of Observations with CTI-2

CTI-2 was tested by operating outside our building at Goddard Space Flight Center. Various scenes were observed, including trees, buildings and other structures, and vehicles. We also imaged the moon in partial phase and during the May 16, 2022 eclipse. Below are selected examples of these observations.

Imaging in two spectral bands. Figure 20 shows distant objects imaged simultaneously in the 4 μm and 10.5 μm spectral bands. This image is a composite of two images with focus adjustments to separately sharpen the nearer objects in the lower half and farther objects in the upper half. The difference in lens position was 0.254 mm. The distances of objects in the scene varied greatly. The tower in the upper portion of the scene was ~650 m from the camera and the handrail in the lower portion was at ~130 m. Although the image was taken during daytime, brightness in the 10.5 μm portion is entirely from thermal emission and in the 4 μm portion is a mixture of thermal and reflected light. Two integration times, listed in Table 4, were applied simultaneously to the two halves of the detector array in order to optimize both of the bandpasses in the same image. Because the 4 μm filter segment was narrow-band and cold, the background in that band was small compared to the dark current. In the 10.5 μm band the background dominated over the dark current. The integration times were chosen to fill the charge wells in both bands to about half-capacity (~6Me-), making the integration time much longer for 4 μm than for 10.5 μm (2.5 ms vs 0.5 ms). With the narrow spectral band, plus the lower photon flux at 4 μm than at 10.5 μm for this ~295K scene, the signal-to-noise is lower in the 4 μm image.

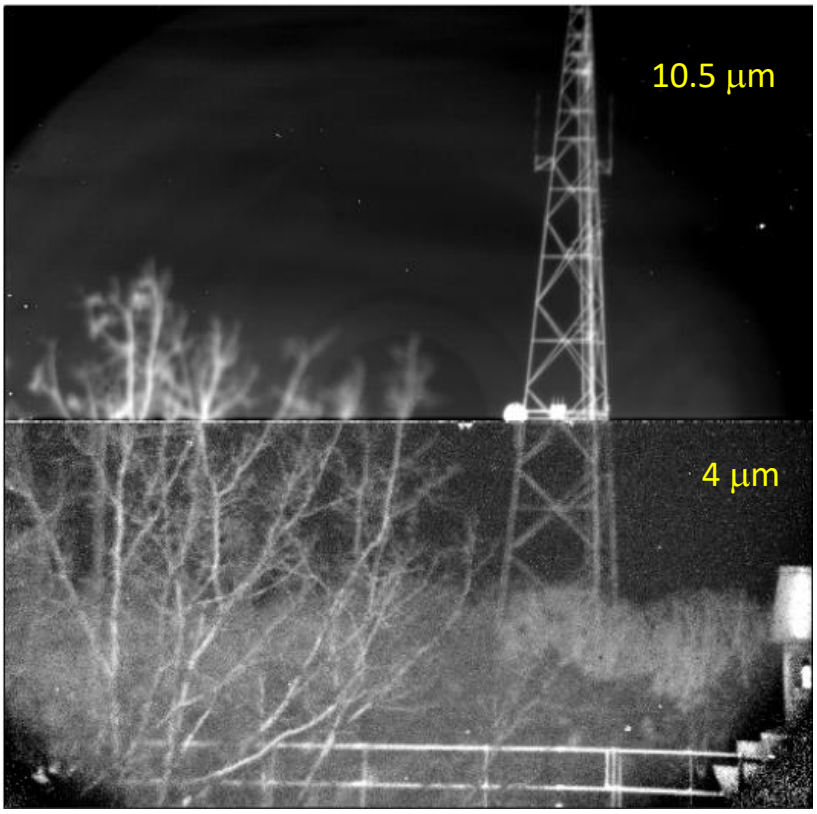

Figure 20. CTI-2 image from both 4 µm and 10.5 µm bands showing objects at a range of distances. Individual segments cover the upper (10.5 µm) and lower (4 µm) halves of the detector array. A focus adjustment was made to optimize the two halves separately. Some telescope vignetting is present in the corners of the frame. Lighter gray corresponds to a higher temperature.

Pushbroom imaging with single-row readout. As an alternative to full-array imaging, as described above, CTI-2 can also be operated in pushbroom mode. In this method a single row of detectors in each spectral band is read out in rapid cadence while the instrument is scanned across the scene. An image is built up in each band as its row gradually samples a swath 1,024 pixels wide and of arbitrarily length. Figures 21 and 22 show examples of pushbroom images from CTI-2. The instrument was attached to a motorized tripod that permitted vertical and horizontal scanning of the field-of-view. The two bands were recorded concurrently by toggling the readout. Integration times were different for the two halves of the detector array, 2.5 and 0.5 msec as listed in Table 4. In this pushbroom mode the signal row was readout every ~17 ms. This pushbroom mode has some advantages over the full-array framing mode. With good cross-track stability an arbitrarily long image can be created along-track. The discontinuities in image mosaics are thereby avoided. The individual rows to be read out can be selected for detector uniformity and operability. When the filter is comprised of two or more filter segments a row can be selected in each segment so that the images in all wavelength are recorded separately in the acquisition step and don't require post-processing.

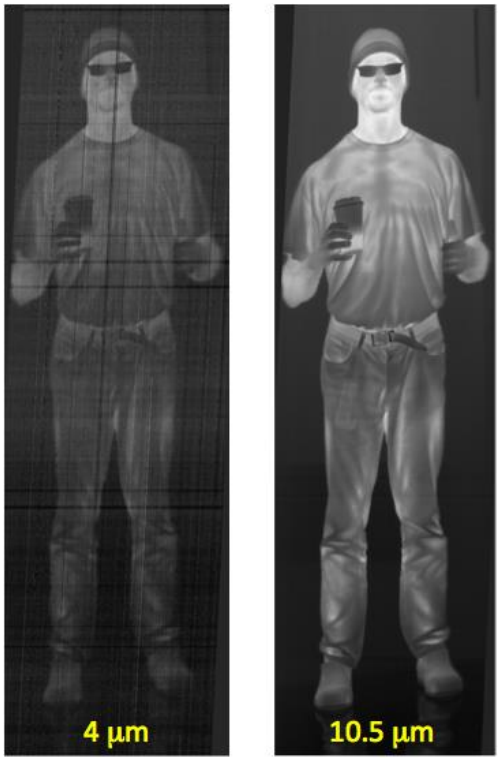

Figure 21. Pushbroom images from the 4 µm and 10.5 µm bands of CTI-2. Images were formed by reading one 1,024-pixel row in each band at rapid cadence while sweeping the camera from top to bottom. Frame integration times are listed in Table 4. Warm liquid in the lower portion of the cup appears as higher temperature (brighter).

The pushbroom method lends itself well to nadir viewing from an orbiting platform, since the projection of the array naturally forms a swath along the ground path. To fully sample along-track the readout cadence is chosen to be less than or equal to the ground pixel dwell time. Readout timing can be set to co-register the images in the multiple bands. Integration times are selected to optimize sensitivity, but not to exceed the ground pixel dwell time. The degree of flexibility of the pushbroom mode is determined by the versatility of the ROIC and the SIDECAR-based control module.

Observations of the Moon. The Moon is an ideal object for testing an infrared spectral imager. Effectively located at infinity, it can serve as a proxy for distant sources, particularly observed from orbit. It is relatively large and can be resolved using modest fore-optics. Plus it is warm, up to 100 C near its sub-solar point, so that it can easily be detected even in the short-wavelength infrared where emission from ~20 C objects is weak. We observed the moon in waxing gibbous phase and during a lunar eclipse to test the long-distance imaging of CTI-2. Figure 23 shows the Moon in both 4 µm and 10.5 µm bands. The Moon was 2 days past first quarter on 13 December 2021. Skies were clear during the observation. CTI-2 was placed on a motorized tripod set at the lunar tracking rate. A focus adjustment was made between the shortwave and longwave images. The variation in thermal brightness across the Moon in the CTI-2 images is due to the dependence of surface temperature on solar illumination. Lunar surface features are not as distinct in the thermal images as they are in visible images.

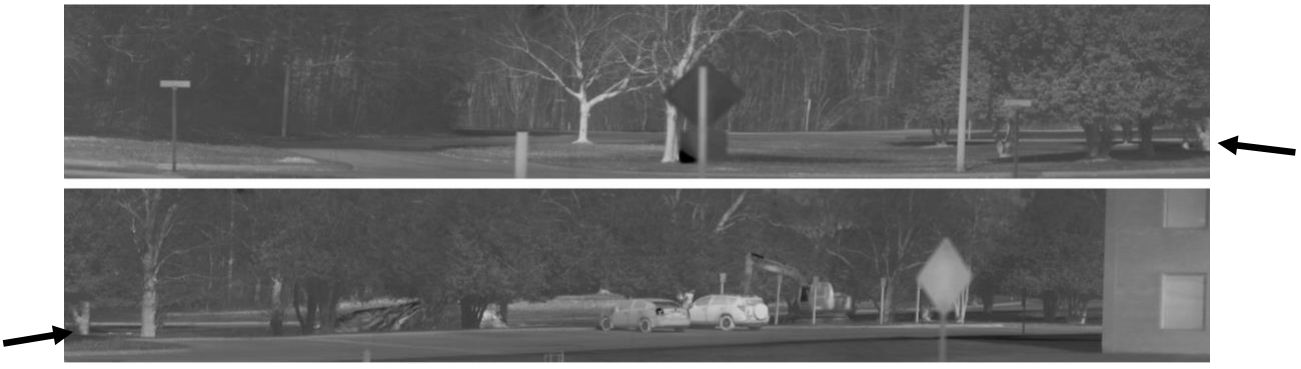

Figure 22. Pushbroom image from the 10.5 mm band of CTI-2. The image was created by repeatedly recording one 1,024-pixel column as the imager was scanned horizontally across the scene. Upper and lower strips are from the same continuous sweep; the rightmost edge of the upper strip overlaps the leftmost edge of the lower strip indicated by the arrows. The frame integration time was 0.5 msec. Lighter gray is higher temperature.

This is because the thermal contrast arises from variations in emissivity and temperature, which have smaller effects than variations in visible albedo. The decreases in thermal brightness away from the subsolar point in the two bands approximately follow a cosine dependence on local solar zenith angle, similar to the dependence of visible illumination on solar angle. Differences in the appearance of the Moon at the two CTI-2 wavelengths are largely due to the greater sensitivity to small temperature differences on the steep shortwave side of the 100 C Plank curve. If we extrapolate our laboratory blackbody calibration to the ~100 C temperature of the subsolar point and compare the expected signal in each band with the observed signal, we find that CTI-2 detected 37% of the lunar emission at 4 μm shortwave and 55% at 10.5 μm. We attribute these losses to atmospheric attenuation.

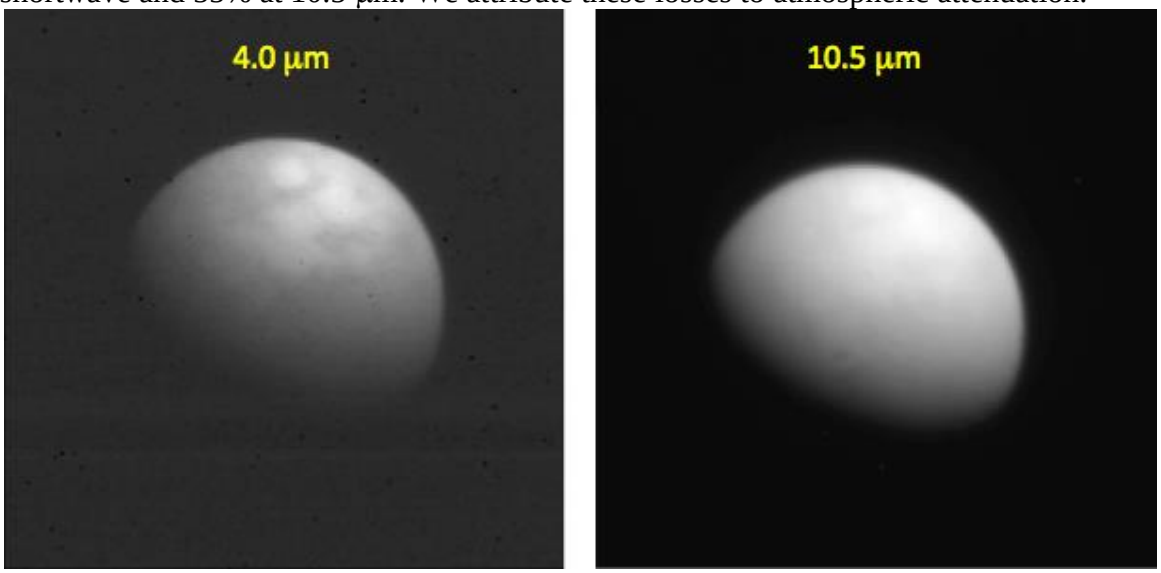

Figure 23. Images of the moon in both the 4.0 μm and 10.5 μm bands recorded on 13 December 2021. Although the signal is weaker at 4 μm than at 10 μm, the thermal contrast at 4 μm is greater between lighter and darker features.

We observed the total eclipse of the Moon with CTI-2 on 16 May 2022. Conditions were generally cloudy, but we were able to record data several times during the second half of the eclipse. We concentrated on the 10.5 μm band for these observations. Figure 24 shows images from several stages of the Moon emerging from Earth's shadow. Brighter is warmer in these images. The leftmost image (04:50 UTC), from the earliest time, was taken near the end of totality and shows surface features in thermal emission with warmer and cooler contrast. The bright spot near the bottom of the image, and another to its left, are craters that have not cooled as rapidly as the rest of the surface during the period in the dark umbra. The two craters are still discernable in the second image (5:12) as totality ends. We examined the brighter crater, Tycho, and found that its brightness temperature was 9 C warmer late in totality (04:50 UTC) and continued to lag by 7 C as the surface warmed (05:42 UTC). Overall, a comparison of visible phase with thermal phase as the Moon returned to full illumination revealed a trailing in thermal brightness by about 15 minutes.

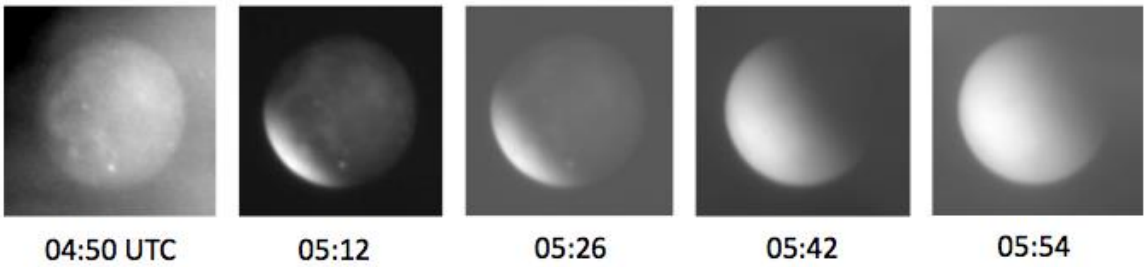

Figure 24. Eclipse of Moon recorded with CTI-2 on 16 May 2022. The Moon was emerging from shadow during these observations. The images are from the 10.5 micron band of the camera. The bright spot near the bottom of the two images at left is the crater Tycho, showed a lag in cooling of the crater after the entering umbra.

V. Conclusion

In our on-going effort to increase our scientific IR imaging capability while reducing size, weight and power we have developed successive generations of ground-based, airborne and space-based IR instruments. As evolution evolved from GaAs QWIP detectors developed and implemented on both the Landsat 8 and Landsat 9 missions to IR facility instruments at both the National Solar Observatory at Kitt Peak and the Big Bear Solar Observatory. With our QWIP camera we supported the 2017 SnowEx aircraft campaign flights, and on another flight we tested our broadband 1kx1k portable SLS camera. We successfully flew our dual-band SLS-based Compact Thermal Imager aboard the RRM-3 payload attached to the International Space Station. We developed a fully integrated six-band multi-spectral 640x512 laboratory camera and are currently building a 1kx1k CubeSat-compatible multi-spectral broad-band imaging system. We continue to leverage the successes of the Small Business Innovative Research programs as well as our own internal R&D resources. As a result of these instrument developments and demonstrations various SLS sensors are being considered for multiple proposals including future Landsat missions [8], remotely monitoring and evaluating fires and improved global health coverage using constellations of CubeSats.

Acknowledgements

We received generous support from the NASA Earth Sciences Technology Office (ESTO), the NASA/Goddard Small Business Innovative Research (SBIR) Office and the NASA/Goddard Internal Research and Development Program (IRAD). Support was also provided by the NASA/USGS Landsat Program. This support helped enable us to not only develop the camera components but also helped us through the difficult times during the pandemic.

References

1. M. D. Jhabvala, D. E. Jennings, C. J. Tucker, A. T. La, B. A. Keer, E. J. Timmons, R. Stone, F. J. Cepollina, A. W. Lunsford, J. Cassidy, M. Sundaram, J. Bundas, W. Squicciarini, P. Finneran, I. Orlowski, C. Fetter, and M. Loose, "Strained-layer-superlattice-based compact thermal imager for the International Space Station," Appl. Opt. **58**(20), 5432-5442 (2019).
2. D. E. Jennings, M. D. Jhabvala, C. J. Tucker, A. W. Lunsford, A. T. La, T. P. Flatley, K. K. Choi, D. L. Wu, D. C. Morton, T. R. Holmes, Y. Fitts, P. G. Cappelaere, A. N. Cillis, K. A. Turck, and T. Hewagama, "Compact Thermal Imager: A Flight Demonstration of Infrared Technology for Earth Observations", *Appl. Opt.* 61, 4215-4225 (2022).
3. K. K. Choi, M. Jhabvala, D. Jennings, K. Turck, A. La, D. Wu, T. Hewagama, T. Holmes, T. Flatley, A. Cillis, Y. Fitts, and D. Morton, "Remote temperature sensing by the Compact Thermal Imager from the International Space Station," Appl. Opt. **60**(33), 10390-10401 (2021).

4. D. L. Wu, D. E. Jennings, K. K. Choi, M. D. Jhabvala, J. A. Limbacher, T. Flatley, K.-M. Kim, A. T. La, R. J. Salawitch, L. D. Oman, J. Gong, T. R. Holmes, D. C. Morton, T. Hewagama, and R. Swap, (2021). "Compact Thermal Imager (CTI) for Atmospheric Remote Sensing," Remote Sens. 2021, 13, 4578. https://doi.org/10.3390/ rs13224578.
5. Jason Bundas, Kelly Patnaude, Richard Dennis, Douglas Burrows, Robert Cook, Axel Reisinger, Mani Sundaram, Robert Benson, James Woolaway, John Schlesselmann, Susan Petronio, "Two-color quantum well infrared photodetector focal plane arrays", Proc. SPIE 6206, Infrared Technology and Applications XXXII, 62060G (2006).
6. M. Burks, C. Cork, D. Eckels, E. Hull, N. Madden, W. Miller, J. Goldsten, E. Rhodes, B. Williams, "Thermal Design and Performance of the Gamma-Ray Spectrometer for the MESSENGER Spacecraft", IEEE Symposium Conference Record Nuclear Science, (2004), p 390.
7. M. Loose, J. Beletic, J. Blackwell, J. Garnett, S. Wong, D. Hall, S. Jacobson, M. Rieke and G. Winters, "The SIDECAR ASIC: focal plane electronics on a single chip," Proc. SPIE 5904, Cryogenic Optical Systems and Instruments XI, 59040V (2005).
8. James R. Irons, John L. Dwyer, and Julia A. Barsi, "The next Landsat satellite: The Landsat Data Continuity Mission", Remote Sensing of Environment 122, 11-21, (2012).